JOURNAL OF THE ROYAL SOCIETY INTERFACE

Foamy oysters: vesicular microstructure production in the Gryphaeidae via emulsification

Journal:	*Journal of the Royal Society Interface*
Manuscript ID	rsif-2020-0505.R2
Article Type:	Research
Date Submitted by the Author:	n/a
Complete List of Authors:	Checa, Antonio; Universidad de Granada, Estratigrafía y Paleontología; Linares, Fátima; Universidad de Granada, Centro de Instrumentación Científica Maldonado-Valderrama, Julia; Universidad de Granada, Departamento de Física Aplicada Harper, Elizabeth; University of Cambridge, Earth Sciences
Categories:	Life Sciences - Physics interface
Subject:	Biomaterials < CROSS-DISCIPLINARY SCIENCES, Biophysics < CROSS-DISCIPLINARY SCIENCES
Keywords:	biomineralization, oysters, vesicular microstructure, solid foam, emulsion, micro-CT

Author-supplied statements

Relevant information will appear here if provided.

Ethics

Does your article include research that required ethical approval or permits?:
This article does not present research with ethical considerations

Statement (if applicable):
CUST_IF_YES_ETHICS :No data available.

Data

It is a condition of publication that data, code and materials supporting your paper are made publicly available. Does your paper present new data?:
My paper has no data

Statement (if applicable):
CUST_IF_YES_DATA :No data available.

Conflict of interest

I/We declare we have no competing interests

Statement (if applicable):
CUST_STATE_CONFLICT :No data available.

Authors' contributions

This paper has multiple authors and our individual contributions were as below

Statement (if applicable):
AGC conceived and designed the study, acquired and analysed data, wrote the paper. FL acquired and analysed data, and revised the paper. JMV analysed data and revised the paper. EMH conceived and designed the study, acquired and analysed data, revised the paper.

Foamy oysters: vesicular microstructure production in the Gryphaeidae via emulsification

Antonio G. Checa[1,2,*], Fátima Linares[3], Julia Maldonado-Valderrama[4], Elizabeth M. Harper[5]

[1]Departamento de Estratigrafía y Paleontología, Universidad de Granada, 18071 Granada, Spain

[2]Instituto Andaluz de Ciencias de la Tierra, CSIC-Universidad de Granada, 18100 Armilla, Spain

[3]Centro de Instrumentación Científica, Universidad de Granada, 18071 Granada, Spain

[4]Departamento de Física Aplicada, Universidad de Granada, 18071 Granada, Spain

[5]Department of Earth Sciences, Cambridge University, CB2 3EQ Cambridge, UK

iD AGC 0000-0001-7873-7545, FL 0000-0003-2205-5953, JMV 0000-0001-6372-723X

*Corresponding author:

e-mail: acheca@ugr.es

Tel. +35 958243201 (office)

+34 635332245 (mobile)

Keywords: biomineralization, oysters, vesicular microstructure, solid foam, emulsion, micro-CT

Running head: vesicular microstructure of oysters

The vesicular microstructure is a very distinctive arrangement of calcite, consisting of hollow cavities (vesicles) of diverse sizes and shapes, usually elongated in the direction of shell thickening. It is uniquely found among living bivalves in a single oyster family, Gryphaeidae. The vesicles are distributed in lenses interleaved with compact foliated layers. We have studied the morphology and distribution of vesicles within the lenses using optical and electron microscopy, and micro-computed tomography. At a small scale, vesicles do not follow a classical von Neumann-Mullins route typical of ideal foams. At a larger scale, the initiation and evolution of a vesicular layer statistically proceed like a foam, with vesicles becoming more numerous, larger, and more even in size. In summary, the vesicular material follows a foam-like coarsening to reduce the number of energetically costly interfaces. However, a steady state is never reached because the animal permanently introduces energy in the system by creating new vesicles. The fabrication of the vesicular material is mediated by the production of an emulsion between the extrapallial fluid and the precursor PILP of the calcitic walls within the thin extrapallial space. For this mechanism to proceed, the mantle cells must perform highly sophisticated behaviours of contact recognition and secretion. Accordingly, the vesicular material is under mixed physical-biological control.

1. Introduction

Calcifying invertebrates have a large repertoire of shell forming microstructures. Molluscs, in particular, show a broad range. These microstructures are a valuable source of inspiration for materials scientists. Most studies have focused on calcified biomaterials with high biomechanical performance (e.g. crossed-lamellar, prismatic calcite) and, sometimes also with economic interest (nacre) [1-3]. Other microstructures have received very little attention, despite raising intriguing fabricational issues. Oysters of the superfamily Ostreoidea comprise several such microstructures. Their shells are entirely calcitic, with the exception of aragonitic myostracal layers and fibres within the ligament [4]. The predominant microstructure is foliated (made of thin continuous layers of sheet-like folia), combined with a thin external columnar prismatic layer (which is thicker on the right than left valve) [5]. In addition though the shells often contain discontinuous lenses of less compact, lower density material, the character of which is different in the two families which make up the Ostreoidea. These intriguing microstructures appear to allow the manufacture of thick shells while reducing either production costs or final weight. In the Ostreidae these patches consist of 'chalk', made with the same type crystalline units (calcitic laths) of units as the foliated material [5], while in the Gryphaeidae the material consists of a highly porous vesicular microstructure (VM) that at least superficially resembles a froth or foam [6]. The focus of this paper is characterizing the VM and building a model for its fabrication.

VM consists of lenses of hollow cavities (vesicles), tens of µm wide, usually elongate, separated by relatively thick (several µm) calcitic walls with polygonal or quasi-polygonal outlines, forming a sort of honeycomb structure (figure 1) [6]. The VM was described already in the early 19th century by DeFrance [7], followed by Douvillé [8] and Ranson [9] in the first half of the past century. Nevertheless, the number of later studies dealing with it is very reduced (see review in [6]). Today there are three surviving genera of Gryphaeidae, all belonging to the subfamily Pycnodonteinae: *Hyotissa*, *Neopycnodonte*, and *Pycnodonte* (which contain a total of nine recognized species [10]). All extant taxa possess VM [11]. Gryphaeid oysters have a long evolutionary history and were particularly diverse and abundant during the Mesozoic [12,13]. Recent evidence suggests that the Pycnodonteinae originated in the Early Cretaceous, and with VM present since at least the Late Cretaceous [14]. There is no suggestion that other extinct gryphaeid subfamilies also secreted VM and hence the character appears to have evolved within the pycnodonteines. Fossil gryphaeids have been important archives for the reconstruction of past climate and environment (e.g. [15-17]). Thus, it is important to understand skeletal formation as it relates to the chronology of skeletal archives.

Hitherto, the only explanation advanced about the mechanism for the fabrication of VM suggests that it is preceded by froth produced by gas bubbles with mucus walls trapped within the extrapallial space (EPS), i.e. between the mantle and the forming shell [6]. The mucus would be later replaced by calcite, with crystallization progressing from the shell wall side towards the mantle. However, this hypothesis has a number of problems. First, the EPS would need to be large to accommodate entire bubbles, whereas we know that it is usually exceedingly thin (<1 µm; e.g. [18]), even during the formation of comparable porous materials, such as the oyster chalk [5]. Second, the vesicles display growth lines (e.g. [19]) which indicate progressive, not the instantaneous growth implied by [6]. Additionally, the vesicles are most often elongated, whereas bubbles are typically spherical to equidimensional polyhedral.

Despite its restricted distribution among the diverse range of microstructures produced by bivalves, VM represents an interesting case from the fabricational viewpoint. How can foam-like material be produced sequentially by the oyster across an extremely thin liquid film (the EPS)? In order to answer this question, we have carried out a study of the vesicular lenses secreted by species of two pycnodonteine genera using scanning electron microscopy (SEM) and micro computed tomography (micro-CT). We have characterized the morphology of the vesicles within the layers and studied their evolution during growth. The results allow us to compare the growth pattern of vesicles in the VM with those of a liquid foam and to propose a model for their fabrication by the oyster, taking into account the space restrictions imposed by the dimensions of the EPS.

2. Material and methods

2.1. Material

We studied specimens of two out of the three genera included within the Pycnodonteinae, in particular, *Hyotissa hyotis* (two specimens, Guadeloupe, France, and the Philippines), *H.* sp. (one specimen, locality unknown) and *Neopycnodonte cochlear* (seven specimens, off the coasts of Greece and southeastern Spain). Additional partial observations were made on *H. mcgintyi* (one specimen, Florida Keys, USA, belonging to the material studied in [20]).

2.2. Optical (OM) and scanning electron microscopy (SEM)

Polished sections as well as fractures of *H. hyotis*, *H.* sp. and *N. cochlear* were cleaned with commercial bleach (approx. 5% active chlorine, for 4–5 min). A few fragments of vesicular lenses were fully decalcified with 4% EDTA to check for any organic remains. Some sections were photographed with a Leica DM1000 LED optical microscope, equipped with a Leica DFC295 camera, belonging to the Department of Stratigraphy and Paleontology of the University of Granada (UGR), Spain. Other sections were additionally imaged by Imagen Científica Ltd. (Granada) with a Sony Alpha A7, equipped with an objective Schneider Componon-s 50. Each final image results from the stacking of 20 to 40 images taken automatically at different focal planes. Samples for SEM observation were coated with carbon (Emitech K975X carbon evaporator) and observed in the field emission SEM (FESEM) equipment Zeiss Auriga and FEI QemScan 650 F of the Centre for Scientific Instrumentation (CIC) of the UGR. Varying magnifications between x40 and x35,000 were employed.

2.3. Micro computed tomography (Micro-CT)

One specimen of each *Hyotissa hyotis*, *H*. sp. and *Neopycnodonte cochlear*, was analysed using X-ray computed axial microtomography (Zeiss Xradia 510 Versa, CIC, UGR). This equipment allows the visualization of distribution patterns of materials with different attenuation values (depending on density and chemical composition) through a reconstruction of sets of parallel cross-sections, perpendicular to the axis of rotation within the scanner. The specimen of *H. mcgintyi* (reposited in the Department of Earth Sciences, Univ. Cambridge) was not available for micro-CT analysis.

The following consistent settings were established to get the same resolution: 4X magnification, 9.5786 µm pixel size, 35 mm source-sample distance, 90 mm detector-sample distance, and 2334 images. Voltage, current, filter and exposure time were adjusted according to particular features of each sample: *Hyotissa hyotis*: 70 kV accelerating voltage (a.v.), 86 μA beam current (b.c.), 9 s exposure time (e.t.) and LE4 source filter (s.f.); *Hyotissa* sp.: 100 kV a.v., 90 μA b. c., 4 s e.t. and LE6 s.f.; *Neopycnodonte cochlear*: 40 kV a.v. and 75 μA b.c., 70 s e.t. and LE2 s.f.. Image reconstruction was done with Reconstructor Scout and Scan™ (Zeiss) using a 0.5 Recon filter and 3201 projections. Dragonfly Pro™ (Object Research System) was used for advanced post-processing analysis and 3D images. Following image binarization, area calculations for vesicles were performed using ImageJ (National Institutes of Health and the Laboratory for Optical and Computational Instrumentation, University of Wisconsin, Madison, WI, USA).

2.4. Thermogravimetric analysis (TGA)

The organic matter contents of one sample of foliated and another of vesicular material of *Hyotissa hyotis*, *Hyotissa* sp. and *Neopycnodonte cochlear* were determined using a thermogravimetric analyser Mettler-Toledo TGA/DSC1 (CIC, UGR). The weight loss was constantly recorded (precision= 0.1 μg) for a temperature range between 23-24°C and 950°C (heating rate= 10°C/min). Significant weight losses between 200°C (when both free and structural water losses are complete) and 600°C (when $CaCO_3$ decomposition into CaO begins) are attributed to the combustion of organic matter.

3. Results

3.1. OM, SEM and TGA

In plan view of the valve interior, the vesicular lenses crop out as irregular or discontinuous bands close to the margin of the upper (right) valve and are covered by compact foliated layers more to the shell interior (figure 1*a-c* and electronic supplementary material, figure S1). In heavily ribbed forms of *Hyotissa*, the vesicular lenses have a periodic distribution, since they appear at the interiors of the ribs and tend to be absent below the intercostal valleys (figure 1*b*, *c* and electronic supplementary material, figure S1*b*, *c*). The vesicular bands are thicker in the ventral area and tend to disappear towards the dorsum (figure 1*a* and electronic supplementary material, figure S1*a*). In the examined species of *Hyotissa* and *Neopycnodonte* both valves develop vesicular lenses, although their thickness and extensions are comparatively reduced in the lower valves.

In section, it can be appreciated that some foliated layers transform into vesicular lenses in the direction toward the margin (figure 1*d*, *e*). At the zone of transformation, the layers/lenses deflect markedly toward the external surface of the shell, to become again parallel to the shell surface at their most marginal portions. This effect is particularly marked in the species of *Hyotissa* (figure 1*d*, *e*). This change in orientation is needed to accommodate the noticeable change in thickness from the foliated to the vesicular material (figure 1*e*, *f*). In this way, the final pattern is that of imbricated vesicular lenses separated by compact foliated layers. This pattern is typical of *Hyotissa*, where lenses are bounded internally and externally by foliated layers. In the right valves of *Neopycnodonte,* the vesicular lenses form immediately underneath the outer prismatic layers close to the margin (figure 1*g*). These prismatic layers transform into foliated in the dorsal direction. On the internal growth surface, it can be appreciated how the interiors of the prisms progressively transform into the calcitic walls of the vesicles, whereas their hollow interiors develop at the positions of the organic membranes surrounding the calcite prisms (figure 2*a*). In both *Hyotissa* and *Neopycnodonte*, the material composing the vesicle walls is an untextured, homogeneous material composed of calcite nanogranules between 50 and 100 nm (figure 2*b*). In *Hyotissa*, there is a vertical transition from the foliated microstructure to the homogeneous microstructure making up the walls of the vesicles (figure 2*c*), whereas, in *Neopycnodonte*, there is no appreciable change in the aspect of the nanostructure between the prisms and vesicles.

In surface views, the vesicles develop polygonal outlines, which are far from regular and/or equidimensional. Sizes may easily change over short distances. Vesicles are separated by thick walls with variable thicknesses (3-30 µm) (figure 2*a*, *d-f*). When the intervening walls are particularly thick, the outlines can be more of the circular or oval type (figure 2*f*). Walls may be straight or bend or wind (figure 1*a*, *d*, *e*). The number of sides of the irregular polygons is also very variable. Walls usually meet at triple points, but some do at quadruple points (figure 2*a*, *d*). There is also a tendency to meet at equal angles, although this is not frequently the case. Vesicular lenses begin with the initiation of a few vesicles, whose size and density increase drastically until a certain lens thickness is reached (figure 2*a*, *d*, *e*). At this early stage, it is easy to observe how a few adjacent vesicles fuse into a larger one (figure 2*a*).

In section, the increase in size with growth is also evident (figure 2*g*, *h*). Vesicles are usually elongated toward the interior thus acquiring a hollow columnar aspect. Columns can frequently change their diameters and disappear/appear (figure 3*a*) in the thickening direction. The surfaces of the walls are imprinted with conspicuous growth lines, which run across vesicles (figures 1*f*, 2*g*-*i*). They clearly mark growth episodes.

Upon decalcification, there is not any appreciable organic remain, which indicates the absence of any internal organic framework. This does not preclude the presence of intracrystalline organic biomolecules, which may have become dispersed in the decalcification solution. This is consistent with the relatively low values of organic matter content recorded by TGA (table 1, and electronic supplementary material, figure S2). The values for the vesicular layer are very similar for the three species analyzed (~2.7% in *H. hyotis*, 2.2% in *H.* sp. and 2.5% in *N. cochlear*). The intervening foliated layers are slightly poorer in organic matter in *H. hyotis* and *H.* sp., and richer in *N. cochlear*. In terms of organic content, the vesicular material is comparable to other relatively organic-poor microstructures, such as the crossed lamellar (e.g. [21]).

3.2. Micro-CT

Our micro-CT results agree with those obtained by SEM. Nevertheless, the former technique provides both sections of the scanned volumes in any direction and 3-D views of the same volumes. In this way, it allows us to ascertain the changes in morphology, size, and density of vesicles during the development of vesicular lenses, with a level of detail much above that of SEM observations. In vertical sections, the distribution of vesicular lenses and interspersed foliated layers is evident. Vesicles also tend to elongate perpendicular to the growth surfaces (figure 3*a*). In horizontal slices, vesicles within a single lens may have very different diameters and, even though their outlines in horizontal section (i.e. roughly parallel the growth surface) tend to be polygonal (due to their close packing), they are extremely variable and irregular. Sometimes, they tend to be more equidimensional and regular (figure 3*b*), although quadruple junctions are relatively common. In other instances, particularly in *N. cochlear*, the patterns are much more irregular (figure 3*c*-*e*). Vesicles may be extremely elongated and irregular; their number of walls ranges from three to >10, and these may be straight or curved. They meet at triple or quadruple points and tend to meet at equal angles, although instances of acute (<90°) and obtuse (>90°), sometimes straight (180°), angles are also frequent. A counting of angles at triple points made on the three measured species shows that the angles of ±120° are more common, although there is a large degree of dispersion both toward higher and lower values (electronic supplementary material, figure S3). Some vesicles contain incomplete walls which extend towards their interiors, or internal isolated walls (figure 3*c*, *e*, *f*). When the sections cut across compact (foliated) layers, it is easy to observe, how the vesicles closer to them tend to have smaller sizes, thicker walls, and more rounded internal outlines (figure 3*b*, *f*-*h*). Away from the foliated layer, vesicle density and mean size increases, at the same time that wall thickness decreases.

3-D views of complete lenses in which only the voids have been shown inform us further about the drastic differences in size and shape of vesicles, giving the aggregates a semi-chaotic appearance (figure 4, and electronic supplementary material, video S1). Vesicles may change in outline from oval elongated perpendicular to the shell thickening direction to rounded, although most commonly tend to be column-like elongated in the direction of shell thickening (i.e. perpendicular to the growth lines; figure 4*a*-*c*). Although shapes easily change within the same lens, the degree of elongation appears to be dependent on the thickness of the lens, with thinner lenses containing more rounded vesicles. Figure 4*c*, taken from a thick lens, shows many examples of elongated vesicles extending for long distances. Our 3-D views clearly show that vesicles not infrequently extend laterally. In this way they meet and fuse with other neighbours, sometimes in sequence (figure 4*a*, *c*, *d*, and electronic supplementary material, video S1). In some instances, the presence of particularly small vesicles at the initiation of a lens is clear (figure 4*e*).

We have carried out two kinds of measurements on micro-CT slices:

(1) In the three species examined we have measured and plotted the changes in cross-sectional area with thickness in small groups of vesicles (between 5 and 10 vesicles per group), in sections approximately parallel to older growth surfaces, indicated by foliated layers similar to those in fig 1*d*-*g* and fig. 3a. Each group consisted of a single cavity (chosen at random) together with all those surrounding it completely. In this way, we can check how particular vesicles relate to their immediate neighbours during growth. In general, plots do not show any defined pattern (figure 5). In some cases, the areas remain steady (figure 5*a*, *b*), or have ascending (figure 5*b*-*d*) or descending trajectories (figure 5*b*, *d*). The trends may reverse and curves take repeatedly fluctuating trajectories (figure 5*e*, *f*), despite the small thicknesses measured (90 µm). The changes in area may proceed smoothly (e.g. figure 5*a*-*d*), or abruptly (figure 5*c*-*f*). We have not found any correspondence between the initial size of the cavity and its trend to increase or decrease: big vesicles may shrink with time (figure 5*b*, *d*-*f*) and the reverse is true for small vesicles (figure 5*b*-*f*). These graphs also register cases of vesicle appearance (figure 5*d*), splitting (a single curve divides into two; figure 5*d*), fusion (two curves fuse into a single one; figure 5*c*, *e*), or cessation (figure 5*d*).

(2) To understand the behaviour of the material at a larger scale, we have tracked the changes of particular parameters with growth on selected areas approximately parallel to older growth surfaces (see paragraph above) containing relatively large numbers of vesicles (from many tens to several hundreds). The parameters measured are: the total area covered by the void part of the vesicles (TA), the number of vesicles (N), their mean surface area (MA), and the variation coefficient of the areas (VC= standard deviation/MA). The latter is a standardized measure of the

polydispersity of the sample, i.e. the dispersion of the areas of vesicles. Measurements have been made across the different slices up to a depth of 600 µm for two different lenses of *H. hyotis* (*H. hyotis* 1 and 2), one of *H.* sp. and one of *N. cochlear*. In this way, we have tracked the variation of those parameters with growth. The curves generated for the four cases analysed are shown in figure 6. The correlations between parameters were analysed to obtain Pearson's Correlation coefficient r and the p value in order to assess the degree of significance in the relationship between them (table 2). In the following discussion we use a value of $p<0.05$ to indicate significance and take $r= 0.7$ as a threshold for strong correlation. Unfortunately, our software did not allow us to calculate volumes of individual vesicles. Estimates of the changes in volume of vesicles with shell thickening might have provided additional relevant information.

In general, the patterns obtained for the four cases show clear differences. In *H. hyotis* 1, *H.* sp and *N. cochlear* the analysed volumes contain partial (*H. hyotis*, *N. cochlear*) or complete (*H*. sp.) transitions from compact (foliated) layers to vesicular lenses (figure 6*a*, *c*, *d*). This is observed in the digitized slices accompanying the plots and is reflected in the fluctuating aspect of the TA curves. In *H. hyotis* 2, the total area fluctuates between narrow values (figure 6*b*).

There is typically a strong significant positive relationship between TA and MA, with high values of $r>0.84$ and $p <0. 00001$ for all except for *H. hyotis 1* where there is no such relationship ($r= 0.341$ and $p= 0.166$). There is only a strong significant positive relationship between TA and N in *H.* sp. In the other cases it appears that increase in total area (TA) is rather compensated by an increase in the mean area (MA) (figure 6*b*, *d*). There is no apparent constant relation between N and MA. Even though the correlation is strongly positively significant for *Hyotissa* sp. the relationship is weakly significant for a negative correlation in the other taxa. The relationship between TA and VC is negative in each case, strongly and significantly for *Neopycnodonte cochlear.* The negative relationship between MA and VC is significant for all (though only after the removal of an outlier in *Hyotissa* sp; figure 6c), strongly so for *N. cochlear.* Finally, N and VC are negatively and significantly related in only two instances (*H. hyotis* 2, *H*. sp.).

In summary, TA, MA, and VC are strongly correlated, while TA and N show some degree of correlation. N is very indirectly related to both MA and VC through TA. The physical explanation is that the increase in total area covered by vesicles is accomplished by increasing the number of vesicles (figure 6*a*, *c*), but preferably also (figure 6*a*, *c*) or exclusively (figure 6*b*, *d*) by increasing the mean area of vesicles. With the increase in total area and number of vesicles, their areas become more even, i.e. the dispersion of vesicle size decreases.

4. Discussion

Vesicular lenses are made from hollow vesicles with polygonal outlines resembling the contours of froth bubbles. This similarity led Stenzel [6] to propose that vesicle formation proceeded via the formation of a foam in the space between the mantle and the shell, which later mineralized. This explanation is not reconcilable with neither the usual dimensions of the EPS in bivalves, much less than a micron in thickness (measured in perpendicular to the mantle surface) [22-28] nor with the morphologies of vesicles usually elongated in the thickening direction (e.g. figure 4). Although we have no direct data, the dimensions of the EPS during the formation of the vesicular lenses cannot be very different from the above value, due to the widespread recognition of growth lines on the inner surfaces of the vesicles, which run across the entire layer (figure 2*g-i*). The growth lines mark the positions of the mantle epithelium surface and indicate that its distance to the forming shell is also very small, certainly, much smaller than the sizes of vesicles. Assuming that growth layers are isochronous and that the distance between them indicates a same time interval, the increase in thickness of the layers (roughly 2-3 times) observed when the foliated material changes into vesicular (figure 1*e*, *f*) indicates that the latter material grows faster in thickness by the observed ratio. This is similar to what was deduced for the chalk produced by the related family Ostreidae [5]. Our decalcification experiments have not revealed any organic residue indicative of a previous organic framework, as found for example in the cuttlebone of *Sepia* [25]. This is consistent with the low amount of organic matter determined with TGA.

4.1. Vesicular layer growth

Our micro-CT data indicate that when we consider groups of vesicles, whatever the species considered, the expansion or contraction of individual vesicles during growth does not obey particular rules (figure 5). Their cross-sectional area may remain steady, increase, or decrease at any rate. Individual vesicles may also appear, disappear, or fuse with other neighbours (see also figure 4). Any of these trends are not at all dependent on the original size of the vesicles. For example, small vesicles may well expand at the expense of larger ones.

Nevertheless, at a larger scale, when we consider areas containing tens to hundreds of vesicles (figure 6), a general trend arises. The initial stages of formation of a vesicular lens immediately below a foliated layer (i.e. toward the interior surface of the valve) are characterized by a few vesicles (as expected) with small and very varied sizes. With the occupation of the area by vesicles (i.e. with the increase in TA), the number of vesicles (N) increases (as expected), but also their mean size (MA), at the same time that their areas become more even (lower VC) (see also figure 3*b*, *f*-*h*). When the whole area is covered by vesicles, there is a phase of stabilization in which these parameters fluctuate within narrow ranges; e.g. the dimensionless VC typically takes values between 0.6-0.8 (figure 6). The observed patterns of fluctuation of sizes and shapes of individual vesicles (figure 5) prevent the system from acquiring higher MA and lower N and VC values.

4.2. Physical model

The outlines of vesicles are often, though not always, reminiscent of those obtained in two-dimensional cellular patterns, such as foams, where boundaries meet in threes at 120° (Plateau's law), which is the condition for surface tension to remain constant throughout the aggregate. Any other configuration would be unstable. However, in the vesicular material, the high incidence of angles significantly different from 120° and of quadruple points (figures 2*a*, *d*, and 3*b*-*d* and electronic supplementary material, figure S3) indicates that it consists of a cellular pattern that is not in equilibrium. The round outlines of vesicles at the initiation of vesicular lenses (figures 2*e*, *f*, and 3*b*, *f*-*h*) are reminiscent of the bubbles formed in wet foams, where the liquid fraction is >10% volume [26]. Later on, vesicles transform into polygonal, which are the typical shapes of bubbles of 2D dry foams (liquid <10% volume). The evolution of liquid foams is governed by three processes: coarsening of bubbles, film thinning and film rupture. Thinning of films between bubbles is due to liquid drainage followed by film rupture. The latter occurs for larger bubbles after reaching a critical film thickness. Liquid foams first drain, then coarsen and, once a critical bubble size is reached, films rupture proceeding to foam destruction. Coarsening occurs owing to differences between bubble pressures which drive inter-bubble gas diffusion. Foams coarsen due to pressure-driven diffusion of gas between bubbles through the liquid phase, resulting in a reduction in the number of bubbles and an increase in their size. Coarsening modifies the size of bubbles and reduces the amount of energetically costly interfaces. In the case of liquid foams, small bubbles disappear at expense of larger ones and, if no new bubbles are created, the total number of bubbles decreases while the average size increases with time. In the case of dry foams, gas exchange occurs directly from bubble to bubble. Since the pressure of bubbles is proportional to curvature, this is affected by the number of neighbours and the change in area is determined by the number of neighbours and not only by size. Coarsening occurs in structured materials organized into cellular domains of a discrete phase dispersed in a second continuous phase, like foams. If the domains can exchange matter, generally by diffusion, the material coarsens in a similar fashion: some domains disappear and the average size of the remaining domains increases [27]. An ideal foam composed of identical bubbles, with the same pressure, would never coarsen. However, real systems always contain some degree of polydispersity which promotes the evolution of bubble size distribution [28].

Cellular patterns arise in phenomena such as foams, emulsions, and metallic grain aggregates, whose dynamics is governed by the von Neumann–Mullins topological law [29,30], which states that those elements with a number of sides greater than six will grow at the expense of those that have less than six sides. In this way, cell number becomes reduced, whereas cell size increases with time [31]. The correlation we have obtained between total area (TA) and the mean area of vesicles (MA) is equivalent to the increase in cell size during the evolution of a 2D foam. Our VC parameter is comparable to the so-called polydispersity measured in foams, which is a measure of the degree of homogeneity of cell-size distribution. There are relatively few studies dealing with the evolution of polydispersity. It was found that foams produced by sparging had an initial ephemerous stage of increasing polydispersity, followed by a permanent decrease in polydispersity [32]. This fits in with the fact that the very initial stage of vesicle formation from the compact foliated later is characterized by high VC values. Then as the vesicular layer develops with the formation of new vesicles that grow in size, they acquire a more homogeneous size distribution, i.e. VC decreases. All in all, from a broad perspective, the growth, in particular the initiation and termination, of vesicular lenses follows a foam-like coarsening dynamics.

Nevertheless, at the scale of individual vesicles, this is not the case. In foams, polydispersed bubbles are more susceptible to coarsening. Larger bubbles increase in size at the expense of smaller ones, which tend to disappear. Only larger bubbles remain at the final stages of foam lifetime, which tend to reach a homogeneous size distribution with minimal free energy. The vesicles of the vesicular lenses, on the contrary, do not follow defined trends (figure 5), and vesicles may enlarge or shrink with time, and either maintain the trend or oscillate, sometimes repeatedly, independently on their original size. This means that the vesicular material can be equated to a cellular pattern-producing phenomenon, which never reaches equilibrium, i.e. it is not a passive process of foam destabilization where there is a trend toward free energy minimisation, as in inorganic systems. Contrarily, VM formation is a dynamic process in which the oyster is introducing energy to the system in the form of changes in bubble shape/size, fission, fusion, initiation, or stopping.

In the living oyster, there is an intervening extremely thin liquid film, the EPS, between the shell-secreting outer mantle and the shell growth surface. Accordingly, we can assume that during the oyster's life, the vesicles are filled with the extrapallial fluid (EPF), such that there is a liquid in contact with the calcified walls of the vesicles (figure 7*a*, *b*). There is presently *in vitro* evidence that biomineralization might proceed by a liquid precursor, namely a polymer-induced liquid precursor (PILP) [33,34], generated by acidic biopolymers during biomineral formation [34-36]. Recently, it has been argued that the PILP is actually a polymer-driven assembly of amorphous calcium carbonate ACC nanoclusters, with liquid-like behaviour [37]. If that was the case in the vesicular microstructure, there would be two liquids in contact at the growth front: the EPF and the PILP (figure 7*b*). If they were relatively immiscible, we would encounter the situation of a bi-liquid foam or emulsion, which is one of the phenomena which obeys the von Neumann-Mullins law. In summary, we propose that the vesicular lenses are formed by the emulsification of the EPF and the liquid precursor of the calcitic walls. It is stressed that the emulsion would only be present within the small thickness (surely submicrometric) where the PILP is present (figure 7*b*). Once this is crystallized into calcite, the morphology produced during the emulsion state becomes permanently 'frozen'.

In *Neopycnodonte*, the outer calcitic columnar prismatic layer transforms into the vesicular layer, with the organic membranes of the former being replaced by the voids of the latter (figure 2*a*). According to the above explanation, the gel-like organic precursor of the membranes would disappear at the transition and would be replaced by the PILP as the continuous phase of the bi-liquid.

If we pay attention to how mantle cells secrete the calcitic walls, there are two options. The first is that the mantle secretes both components (EPF and PILP) homogeneously all along its surface. Later the PILP component travels to the adequate positions at the growth fronts of the walls. However, we are unaware of any physical process by which the PILP clusters can travel for large distances (tens of µm) across a nanometric EPS until they find a mineral wall. Moreover, in those areas where the cells are facing vesicles, PILP clusters would disperse within the interior of the vesicles and produce 'undesired' mineralization.

The alternative possibility is that the cells are able to directly secrete the PILP at the positions of the walls of the vesicles. Bivalve mantle cell sizes (5-10 µm) [38-40] are, in general, bigger than the thickness of cavity walls (2-10 µm) and well below the diameters of vesicles (<10 to >100 µm) (figure 2). This implies that some cells will be entirely within the interior of vesicles (i.e., secreting only EPF), whereas others will be secreting wall segments (PILP) only along their surfaces in contact with the wall. In this way, several mantle cells will cooperate in the production of an entire wall. That is, every mantle cell will be secreting either PILP of EPF at different positions on its surface depending on which structure it is in contact with (figure 7b). Cells only partly in contact with the walls will be secreting bot PILP (at the contact with the wall) and EPF (at the contact with the cavity). Since the mantle slides past the shell growth surface during periods of non-deposition (figure 7*a*), the cells must regain information on the exact placement of the previously secreted structures when shell deposition resumes (figure 7*b*) by some kind of spatial recognition process. Accordingly, mantle cells must be able to both collect this information and secrete materials at the subcellular level. Similar situations were proposed for the secretion of other molluscan materials, such as the calcitic columnar prismatic layers of bivalves [41] and the aragonitic fibrous spiral microstructure of some gastropods [42]. A similar strict cellular control has been proposed for the production of the calcitic fibrous layer of brachiopods [43].

Recognition phenomena by cells is a widespread phenomenon, with profound effects in many biological processes, like aggregation, growth, immune response, etc. [44]. Cells are able to recognize other cells (of the same or of a different organism), but also substrates of different kinds [45,46]. Recognition is carried out by means of surface molecules (receptors), able to recognize particular biomolecules (ligands) present on the neighbor cellular wall or on the substrate. This mechanism extends to mollusc cells [47]. This ability is used in biomaterial science to activate inert biomaterial surfaces by coating them with natural extracellular matrix proteins able to be recognized by cells [48]. In this way, some natural biomaterials (such as nacre) develop important bioadhesive and biocompatible properties. I particular, they stimulate osteoblast growth and secretory activity [49,50]. Osteoblasts are also able recognize different nacre topographies [51]. Although we do not have direct evidence, it becomes clear that the oyster mantle cells could well differentiate walls from cavities and secrete either PILP or EPF accordingly.

In summary, the fabrication of the vesicular material is mediated by the production of an emulsion between the EPF and the precursor PILP of the calcitic walls. This initial emulsion later crystallizes leaving foam-like morphologies. At the same time, the mantle cells are able to develop incredibly sophisticated behaviours of contact recognition and secretion, in areas smaller than their entire surfaces. Accordingly, the vesicular material is under a mixed physical-biological control.

Data accessibility. Supplementary figures S1 to S3 and Supplementary video S1 has been uploaded as part of the electronic supplementary material.

Authors' Contributions. AGC conceived and designed the study, acquired and analysed data, wrote the paper. FL acquired and analysed data, and revised the paper. JMV analysed data and revised the paper. EMH conceived and designed the study, acquired and analysed data, revised the paper.

Competing interests. We have no competing interests.

Acknowledgements. We thank Dr. Sonia Ros (Facultad de Ciencias Naturales and Museo de La Plata, Universidad Nacional de La Plata, Argentina) for advice on fossil gryphaeid oysters.

Funding. This research was funded by projects CGL2017-85118-P of the Spanish Ministerio de Ciencia e Innovación, the Unidad Científica de Excelencia UCE-PP2016-05 of the University of Granada and the Research Group RNM363 of the Junta de Andalucía.

References

1. Jackson P, Vincent JFV, Turner RM. 1988 The mechanical design of nacre. *Proc. R. Soc. London B* **234**, 415–440. (doi:10.1098/rspb.1988.0056)

2. Ji H, Li X, Chen D. 2017 *Cymbiola nobilis* shell: Toughening mechanisms in a crossed-lamellar structure. *Sci Rep* **7**, 40043. (doi:10.1038/srep40043)

3. Strąg M, Maj Ł, Bieda M, Petrzak P, Jarzębska A, Gluch J, Topal E, Kutukova K, Clauser A, Heyn W, et al. 2020 Anisotropy of mechanical properties of *Pinctada margaritifera* mollusk shell. *Nanomaterials* **10**, 634. (doi:10.3390/nano10040634)

4. Dungan CF. 2008 Aragonite-fiber calcification of the hinge ligament mechanical antagonist to valve adduction in oysters. *J. Shellfish Res.* **27**, 1004. (doi:10.2983/0730-8000(2008)27[985:AOTPPA]2.0.CO;2)

5. Checa AG, Harper EM, González-Segura A. 2018 Structure and crystallography of foliated and chalk shell microstructures of the oyster *Magallana*: the same materials grown under different conditions. *Sci. Rep.* **8**, 7507. (doi:10.1038/s41598-018-25923-6)

6. Stenzel HB. 1971 Oysters. In *Treatise on invertebrate paleontology, part N, vol. 3, Mollusca 6, Bivalvia* (ed RC Moore), pp. 953–1224. Lawrence, K: Geological Society of America and University of Kansas Press.

7. Defrance M. 1821 Huitres (Foss.) In *Dictionnaire des sciences naturelles, vol 22*, pp. 20-33. Paris: FG Levrault.

8. Douvillé H. 1936 Le test des ostréidés du groupe de l'*Ostrea cochlear* (genre *Pycnodonta*, F. de W.). *C. R. Hebdm. Séances Acad. Sci Paris* **203**, 1113-1117.

9. Ranson G. 1941 Les espèces actuelles et fossils du genre *Pycnodonta* F. de W.: 1. *Pycnodonta hyotis* (L.). *Bull. Mus. Natl. Hist. Nat. Paris* **13**, 82-92.

10. MolluscaBase (eds) 2020 MolluscaBase. Pycnodonteinae Stenzel, 1959. Accessed through: World Register of Marine Species at: http://www.marinespecies.org/aphia.php?p=taxdetails&id=510709 on 2020-04-13

11. Harry H. 1985 Synopsis of the supraspecific classification of living oysters (Bivalvia: Gryphaeidae and Ostreidae). *Veliger* **28**, 121–158.

12. Hallam A. 1982 Patterns of speciation in Jurassic *Gryphaea*. *Paleobiology* **8**, 354-366. (doi: 10.1017/S0094837300007107)

13. Jablonski D, Bottjer DJ. 1983 Soft-bottom epifaunal suspension-feeding assemblages in the Late Cretaceous. In *Biotic Iinteractions in recent and fossil benthic communities. Topics in Geobiology, vol. 3* (eds MJS Tevesz, PL McCall), pp. 747-812. Boston, MA: Springer.

14. Kosenko I. 2018 The origin of the Pycnodonteinae and relationship between gryphaeas and true pycnodontes. *Acta Palaeontol. Pol.* **63**, 769–778. (doi:10.4202/app.00494.2018)

15. Meyer KW, PetersenSV, Lohmann KC, Blum JD, Washburn SJ, Johnson MW, Gleason JD, Kurz AY, Winkelstern IZ. 2019 Biogenic carbonate mercury and marine temperature records reveal global influence of Late Cretaceous Deccan Traps. *Nat. Comm*. **10**, 5356. (doi: 10.1038/s41467-019-13366-0)

16. de Winter NJ, Vellekoop J, Vorsselmans R, Golreihan A, Soete J, Petersen SW, Meyer KW, Casadio S, Speijer RP, Claeys P. 2018 An assessment of latest Cretaceous *Pycnodonte vesicularis* (Lamarck, 1806) shells as records for palaeoseasonality: a multi-proxy investigation. *Clim. Past* **14**, 725–749. (doi:10.5194/cp-14-725-2018)

17. Hesselbo SP, Korte C, Ullmann CV, Ebbesen AL. 2020 Carbon and oxygen isotope records from the southern Eurasian Seaway following the Triassic-Jurassic boundary: Parallel long-term

enhanced carbon burial and seawater warming. *Earth Sci. Rev.* **203**, 103131. (doi:10.1016/j.earscirev.2020.103131)

18. Checa A. 2018 Physical and biological determinants of the fabrication of molluscan shell microstructures. *Front. Mar. Sci.* **5**, 353. (doi:10.3389/fmars.2018.00353)

19. Tischak J, Zuchin M, Spötl C, Baal C. 2010 The giant oyster *Hyotissa hyotis* from the northern Red Sea as a decadal-scale archive for seasonal environmental fluctuations in coral reef habitats. *Coral Reefs* **29**, 1061–1075. (doi:10.1007/s00338-010-0665-7)

20. Bieler R, Mikkelsen PM, Collins TM, Glover EA, González VL, Graf DL, Harper EM, Healy J, Kawauchi GY, Sharma PP, et al. 2014 Investigating the Bivalve Tree of Life: an exemplar-based approach combining molecular and novel morphological characters. *Invertebr. Syst.* **28**, 32–115. (doi:10.1071/IS130 10)

21. Agbaje OBA, Thomas DE, Dominguez JG, Mclnerney BV, Kosnik MA, Jacob DE. 2019 Biomacromolecules in bivalve shells with crossed lamellar architecture. *J. Mater. Sci.* **54**, 4952–4969. (doi:10.1007/s10853-018-3165-8)

22. Nakahara H, Bevelander G. 1971 The formation and growth of the prismatic layer of *Pinctada radiata*. *Calcif. Tissue Res.* **7**, 31–45. (doi:10.1007/BF02062591)

23. Cartwright JHE, Checa AG. 2007 The dynamics of nacre self-assembly. *J. R. Soc. Interface* **4**, 491–504. (doi:10.1098/rsif.2006.0188)

24. Checa AG, Salas C, Harper EM, Bueno-Pérez JD. 2014 Early stage biomineralization in the periostracum of the 'living fossil' bivalve *Neotrigonia*. *PLoS One* **9**, e90033. (doi:10.1371/journal.pone.0090033)

25. Checa AG, Cartwright JHE, Sánchez-Almazo I, Andrade JP, Ruiz-Raya F. 2015 The cuttlefish *Sepia officinalis* (Sepiidae, Cephalopoda) constructs cuttlebone from a liquid-crystal precursor. *Sci. Rep.* **5**, 11513. (doi:10.1038/srep11513)

26. Langevin D. 2017 Aqueous foams and foam films stabilised by surfactants. Gravity-free studies. *C. R. Mecanique* **345**, 47-55. (doi:10.1016/j.crme.2016.10.009)

27. Cantat I, Cohen-Adad S, Elias F, Graner F, Höhler R, Pitois O, Rouyer F, Saint-Jalmes A, Cox S. 2013 Foams: structure and dynamics. Oxford, UK: Oxford University Press.

28. Drenckhan W, Langevin D. 2010 Monodisperse foams in one to three dimensions. *Curr. Opin. Colloid Interface Sci.* **15**, 341–358. (doi:10.1016/j.cocis.2010.06.002)

29. von Neumann J. 1952 Written discussion on a paper of C. S. Smith. In *Metal interfaces* (ed. C Herring), pp. 108–110. Cleveland, OH: American Society of Metals.

30. Mullins WW. 1956 Two-dimensional motion of idealized grain boundaries. *J. Appl. Phys.* **27**, 900–904. (doi:10.1063/1.1722511)

31. Isert N, Maret G, Aegerter CM. 2013 Coarsening dynamics of three-dimensional levitated foams: From wet to dry. *Eur Phys J E* **36**, 116. (doi:10.1140/epje/i2013-13116-x)

32. Kann KB. 2006 Quantitative estimation of polydispersity of gas–liquid foams. *Coll. Surf. A* **287**, 237–241. (doi:10.1016/j.colsurfa.2006.03.041)

33. Gower LB, Odom DJ. 2000 Deposition of calcium carbonate films by a polymer-induced liquid-precursor (PILP) process. *J. Cryst. Growth* **210**, 719–734. (doi:10.1016/S0022-0248(99)00749-6)

34. Gower LB. 2008 Biomimetic model systems for investigating the amorphous precursor pathway and its role in biomineralization. *Chem. Rev.* **108**, 4551–4627. (doi:10.1021/cr800443h)

35. Schenk AS, Zope H, Kim Y-Y, Kros A, Sommerdijk NAJM, Meldrum FC. 2012 Polymer-induced liquid precursor (PILP) phases of calcium carbonate formed in the presence of synthetic acidic polypeptides—relevance to biomineralization. *Faraday Discuss.* **159**, 327–344. (doi:10.1039/c2fd20063e)

36. Wolf SE, Lieberwirth I, Natalio F, Bardeau J-F, Delorme N, Emmerling F, Barrea R, Kappl M, Marin F. 2012 Merging models of biomineralisation with concepts of nonclassical crystallisation: is a liquid amorphous precursor involved in the formation of the prismatic layer of the Mediterranean fan mussel *Pinna nobilis*? *Faraday Discuss.* **159**, 433–448. (doi:10.1039/c2fd20045g)

37. Xu Y, Tijssen KCH, Bomans PHH, Akiva A, Friedrich H, Kentgens APM, Sommerdijk NAJM. 2018 Microscopic structure of the polymer-induced liquid precursor for calcium carbonate. *Nat. Comm.* **9**, 2582. (doi:10.1038/s41467-018-05006-w)

38. Beedham GE. 1958. Observations on the mantle of the Lamellibranchia. *Q. J. Microsc. Sci.* **99**, 181–197.

39. Bevelander G, Nakahara H. 1967 An electron microscopy study of the formation of the periostracum of *Macrocallista maculata*. *Calcif. Tissue Res.* **1**, 55–67.

40. Bubel A. 1973 An electron-microscope study of periostracum formation in some marine bivalves. II. The cells lining the periostracal groove. *Mar. Biol.* **20**, 222–234. (doi:10.1007/BF00348988)

41. Checa AG, Macías-Sánchez E, Harper EM, Cartwright JHE. 2016 Organic membranes determine the pattern of the columnar prismatic layer of mollusc shells. *Proc. R. Soc. B* **283**, 20160032. (doi:10.1098/rspb.2016.0032)

42. Checa AG, Macías-Sánchez E, Ramírez-Rico J. 2016 Biological strategy for the fabrication of highly ordered aragonite helices: the microstructure of the cavolinioidean gastropods. *Sci. Rep.* **6**, 25989. (doi:10.1038/srep25989)

43. Simonet-Roda M, Griesshaber E, Ziegler A, Rupp U, Yin X, Häussermann V, Laudien J, Brand U, Eisenhauer A, Checa AG, Schmahl WW. 2019. Calcite fibre formation in modern brachiopod shells. *Sci. Rep.* **9**, 598. (doi:10.1038/s41598-018-36959-z)

44. Saier MH, Jacobson GR. 1984 Cellular recognition: mechanisms and consequences of homotypic and heterotypic adhesions. In: *The molecular basis of sex and differentiation* (eds MH Saier, GR Jacobson), pp. 135-157. New York, NY: Springer. (doi:10.1007/978-1-4612-5260-3_10)

45. Culp LA. 1978 Biochemical determinants of cell adhesion. *Curr. Topics Membr. Transp.* **11**, 327-396. (doi:10.1016/S0070-2161(08)60752-2)

46. Obrink B, Ocklind C. 1983 Cell-cell recognition: relation to cell adhesion with special reference to adhesion of hepatocytes. *Blood Cells* **9**, 209-219.

47. Gerdol M, Gomez-Chiarri M, Castillo MG, Figueras A, Fiorito G, Moreira R, Novoa B, Pallavicini A, Ponte G, Roumbedakis K, et al. 2018 Immunity in molluscs: recognition and effector

mechanisms, with a focus on Bivalvia. In: *Advances in comparative immunology* (ed EL Cooper), pp, 225-341. Cham, Switzerland: Springer. (doi.org/10.1007/978-3-319-76768-0_11)

48. Rahmany MB, Van Dyke M. 2013 Biomimetic approaches to modulate cellular adhesion in biomaterials: A review. *Acta Biomater.* **9**, 5431–5437. (doi: 10.1016/j.actbio.2012.11.019)

49. Lopez E, Vidal S, Berland S, Camprasse G, Camprasse C, Silve C. 1992 Demonstration of the capacity of nacre to induce bone formation by human osteoblasts maintained in vitro. *Tissue Cell* **24**, 667-679. (doi:10.1016/0040-8166(92)90037-8)

50. Waddell SJ, de Andrés MC, Tsimbouri PM, Alakpa EV, Cusack M, Dalby MJ, Oreffo ROC. 2018 Biomimetic oyster shell–replicated topography alters the behavior of human skeletal stem cells. *J. Tissue Eng.* **9**, 1–13. (doi: 10.1177/2041731418794007)

51. Alakpa EV, Burgess KEV, Chung P, Riehle MO, Gadegaard N, Dalby MJ, Cusack M. 2017 Nacre topography produces higher crystallinity in bone than chemically induced osteogenesis. *ACS Nano* **11**, 6717−6727. (doi: 10.1021/acsnano.7b01044)

Figure captions

Figure 1. Distribution of vesicular lenses in the shells of Pycnodonteinae. *(a)* Interior of an upper valve of *Hyotissa hyotis*, showing the marginal distribution of the vesicular material. *(b)*, *(c)* details of the two areas indicated in *(a)*. The vesicular material is preferentially distributed within the rib concavities. *(d)* Longitudinal sections along a rib (top) and the adjacent intercostal valley (bottom) of *Hyotissa hyotis*, showing the difference in the development of vesicular lenses, which are virtually absent in the bottom section. *(e)* Detail of a section similar to that in *(d)* with indication of some growth lines (broken lines). The thickness between growth lines clearly increases from the compact foliated to the hollow vesicular material. *(f)* SEM view of a transversal section of a rib. Growth lines are indicated with broken lines. There is an increase in the thickness between growth lines towards the more porous areas (top of rib). *(g)* Section along the margin of *Neopycnodonte cochlear*. The vesicular lenses develop immediately below prismatic layers, which, more to the shell interior change into foliated layers. f: foliated layer; p: prismatic layer; v: vesicular lens. See clean magnifications of (*a*), (*b*) and (*c*) in electronic supplementary material, figure S1*a*, *b* and *c*, respectively.

Figure 2. SEM details of vesicular lenses. *(a)* View of the internal surface of a right valve of *Neopycnodonte cochlear* at the transition from the outer prismatic layer (pl, right) to the vesicular layer (vl, left). The positions of some organic membranes of the prismatic layer are indicated with short arrows. 'f' indicates cases of fusion of small vesicles into a larger one and 'q' indicates quadruple points. *(b)* Nanogranular aspect of the wall of a cavity of *Hyotissa* sp. *(c)* Transition between the foliated layer (right) and the underlying vesicular layer of *Hyotissa* sp. *(d)* Internal growth surface of *Hyotissa hyotis*. The contact with the outer foliated layer is toward the bottom. With the development of the vesicular layer, the vesicles increase in size. Some walls meet at quadruple points (q). *(e)* Similar situation in *Neopycnodonte cochlear*. *(f)* Growth surface of the vesicular layer in *Hyotissa* sp. The walls are particularly thick and the vesicles have rounded outlines. *(g)*, *(h)* Fractures through the vesicular lenses of *Hyotissa hyotis* and *Hyotissa* sp. The size of vesicles increases in the thickening direction (toward the bottom in *(g)* and toward the left in *(h)*). Conspicuous growth lines (arrows) are imprinted on the interior of vesicles (arrows) and run across them. *(i)* Fracture through the vesicular layer of *Hyotissa mcgintyi*. Growth lines run across vesicles (arrows). Big arrows in *(a)* and *(c)*-*(i)* indicate the direction toward the margin.

Figure 3. Micro-CT slices showing the aspect of vesicular lenses. *(a)* Section perpendicular to the shell surface through the shell margin of *Hyotissa hyotis*, showing the distribution of vesicular lenses and some intervening foliated layers. Note elongation of vesicles parallel to the shell thickening direction. *(b)*-*(h)* Sections approximately parallel to the shell surface of the vesicular material of *Hyotissa hyotis* (*(b)*), *Neopycnodonte cochlear* (*(c)*-*(f)*) and *Hyotissa* sp. (*(g)*,*(h)*). *(b)*

Relatively regular polygonal pattern. Arrows point to some quadruple connections. *(c)-(e)* Extremely irregular polygonal patterns. Arrows point to incomplete walls (*(c), (e)*), sometimes isolated within vesicles (*(e)*). *(f)-(h)* Views including transitions between foliated layers and vesicular lenses. The very transitions are marked by smaller vesicles, with thicker walls and more rounded outlines. Red arrows in *(f)* point to walls that are incomplete or became isolated within cell interiors. f: foliated layer.

Figure 4. 3D views of the hollow interiors of vesicles of *Hyotissa hyotis* (*(a)-(c)*) and *Neopycnodonte cochlear* (*(d),(e)*). In all cases, the vesicles elongate perpendicular to the growth lines (marked with broken lines in *(a)* and *(b)*). The close ups in *(a)* and *(c)-(e)* are intended to show the high irregularity in vesicle size and shape, and the high degree of interconnections between vesicles. The close up in *(e)* also shows the high number of small vesicles at the initiation of the lower vesicular lens.

Figure 5. Changes in surface area in groups of contiguous vesicles in *Hyotissa hyotis* (*(a)*), *Hyotissa* sp. (*(c)*, *(e)*, *(f)*) and *Neopycnodonte cochlear* (*(b)*, *(d)*). The plots have been arranged according to the pattern. *(a)*, *(b)*. Slightly fluctuating cavity areas. *(c)*. Increasing areas. The upper yellow curve differs from the rest in its step-like shape. *(d)*. Mixed pattern with decreasing and increasing areas. *(e)*, *(f)* Strongly fluctuating areas. Positions indicated with 'a', 'c', 'f' and 's' indicate appearance, cessation, fusion, and splitting of vesicles, respectively. The top images are binarized micro-CT images of the groups taken at the indicated positions (void areas in black and walls in white). Increase in thickness is towards the internal surface of the shell in all cases.

Figure 6. Evolution across the shell thickness of the mentioned parameters: total area occupied by vesicles (TA), number of vesicles (N), mean area of vesicles (MA) and coefficient of variation of the areas of individual vesicles (VC) in selected areas (see dimensions above each graph) of *(a) Hyotissa hyotis* 1*, (b) Hyotissa hyotis* 2, *(c) Hyotissa* sp., and (d) *Neopycnodonte cochlear*. Note general positive covariation between TA and MA, and negative covariation between MA and VC. The position indicated with an asterisk in *(c)* is an anomalous value (see text). The top images are digitized micro-CT images taken at different depths (void areas in black and walls in white). Percentages associated to the TA curves are the percent of TA with respect to the whole framed area. Increase in thickness is towards the internal surface of the shell in all cases.

Figure 7. Model for the fabrication of the vesicular materials in gryphaeids. During the oyster's life, the vesicles are infilled with extrapallial fluid. *(a)* During non-secretory periods, the mantle is able

to move with respect to the growth surface of the vesicular shell material (black wide arrows). *(b)* When shell growth resumes, the mantle cells adhere to the growth surface. Then, they are able to sense the grid formed by the growth ends of the walls (red arrows) and secrete a PILP phase directly and exclusively onto them. With time the PILP crystallizes into calcite.

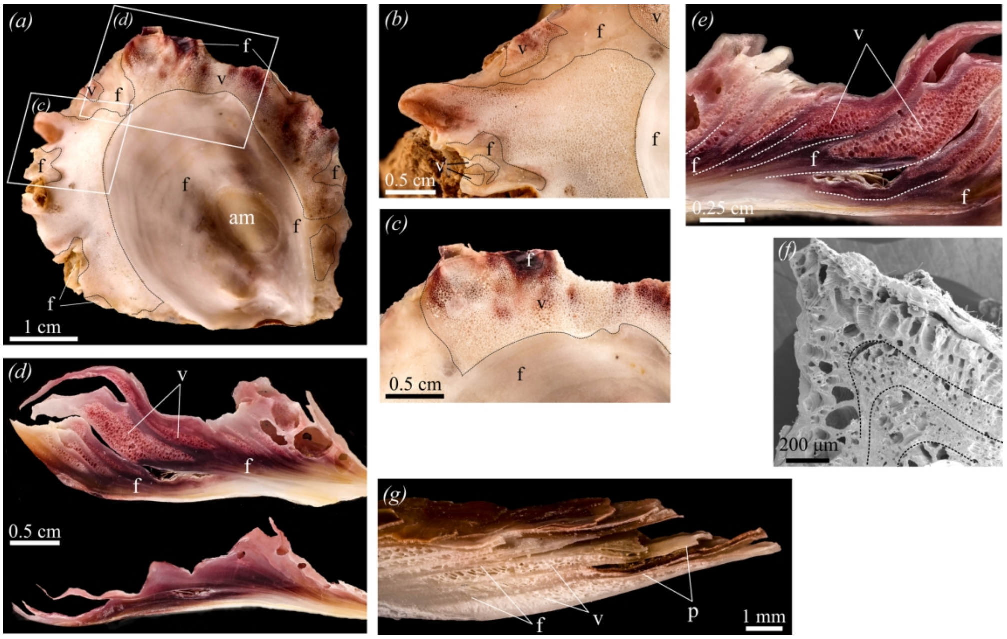

Figure 1. Distribution of vesicular lenses in the shells of Pycnodonteinae. (a) Interior of an upper valve of Hyotissa hyotis, showing the marginal distribution of the vesicular material. (b), (c) details of the two areas indicated in (a). The vesicular material is preferentially distributed within the rib concavities. (d) Longitudinal sections along a rib (top) and the adjacent intercostal valley (bottom) of Hyotissa hyotis, showing the difference in the development of vesicular lenses, which are virtually absent in the bottom section. (e) Detail of a section similar to that in (d) with indication of some growth lines (broken lines). The thickness between growth lines clearly increases from the compact foliated to the hollow vesicular material. (f) SEM view of a transversal section of a rib. Growth lines are indicated with broken lines. There is an increase in the thickness between growth lines towards the more porous areas (top of rib). (g) Section along the margin of Neopycnodonte cochlear. The vesicular lenses develop immediately below prismatic layers, which, more to the shell interior change into foliated layers. f: foliated layer; p: prismatic layer; v: vesicular lens. See clean magnifications of (a), (b) and (c) in electronic supplementary material, figure S1a, b and c, respectively.

164x104mm (300 x 300 DPI)

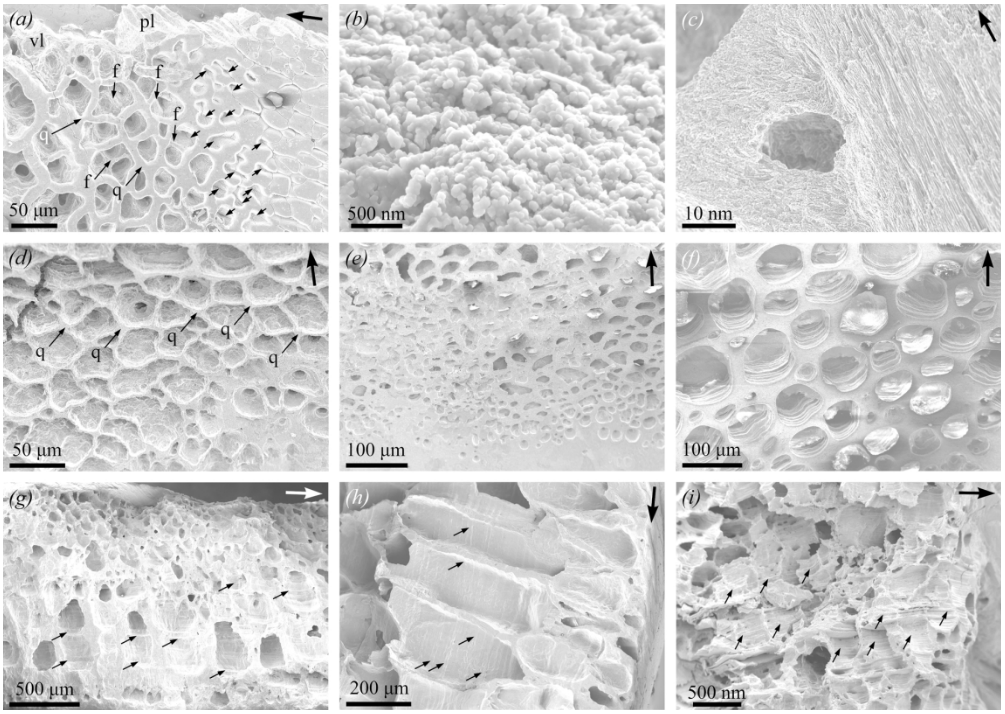

Figure 2. SEM details of vesicular lenses. (a) View of the internal surface of a right valve of Neopycnodonte cochlear at the transition from the outer prismatic layer (pl, right) to the vesicular layer (vl, left). The positions of some organic membranes of the prismatic layer are indicated with short arrows. 'f' indicates cases of fusion of small vesicles into a larger one and 'q' indicates quadruple points. (b) Nanogranular aspect of the wall of a cavity of Hyotissa sp. (c) Transition between the foliated layer (right) and the underlying vesicular layer of Hyotissa sp. (d) Internal growth surface of Hyotissa hyotis. The contact with the outer foliated layer is toward the bottom. With the development of the vesicular layer, the vesicles increase in size. Some walls meet at quadruple points (q). (e) Similar situation in Neopycnodonte cochlear. (f) Growth surface of the vesicular layer in Hyotissa sp. The walls are particularly thick and the vesicles have rounded outlines. (g), (h) Fractures through the vesicular lenses of Hyotissa hyotis and Hyotissa sp. The size of vesicles increases in the thickening direction (toward the bottom in (g) and toward the left in (h)). Conspicuous growth lines (arrows) are imprinted on the interior of vesicles (arrows) and run across them. (i) Fracture through the vesicular layer of Hyotissa mcgintyi. Growth lines run across vesicles (arrows). Big arrows in (a) and (c)-(i) indicate the direction toward the margin.

164x116mm (300 x 300 DPI)

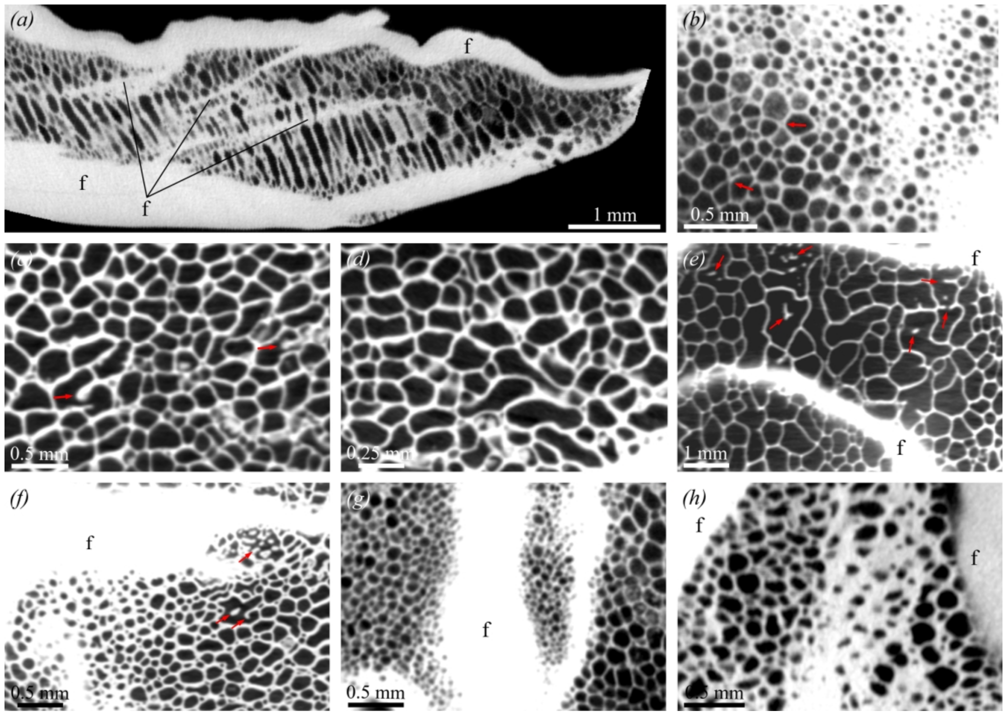

Figure 3. Micro-CT slices showing the aspect of vesicular lenses. (a) Section perpendicular to the shell surface through the shell margin of Hyotissa hyotis, showing the distribution of vesicular lenses and some intervening foliated layers. Note elongation of vesicles parallel to the shell thickening direction. (b)-(h) Sections approximately parallel to the shell surface of the vesicular material of Hyotissa hyotis ((b)), Neopycnodonte cochlear ((c)-(f)) and Hyotissa sp. ((g),(h)). (b) Relatively regular polygonal pattern. Arrows point to some quadruple connections. (c)-(e) Extremely irregular polygonal patterns. Arrows point to incomplete walls ((c), (e)), sometimes isolated within vesicles ((e)). (f)-(h) Views including transitions between foliated layers and vesicular lenses. The very transitions are marked by smaller vesicles, with thicker walls and more rounded outlines. Red arrows in (f) point to walls that are incomplete or became isolated within cell interiors. f: foliated layer.

164x116mm (300 x 300 DPI)

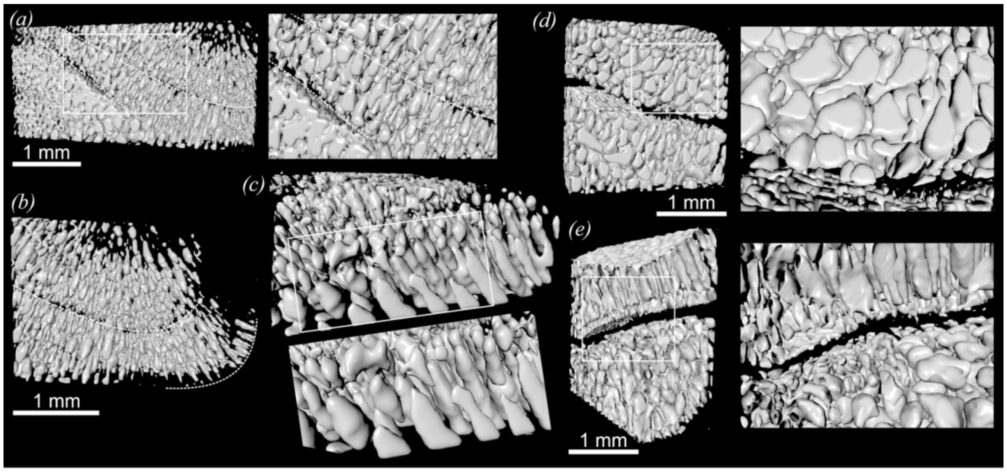

Figure 4. 3D views of the hollow interiors of vesicles of Hyotissa hyotis ((a)-(c)) and Neopycnodonte cochlear ((d),(e)). In all cases, the vesicles elongate perpendicular to the growth lines (marked with broken lines in (a) and (b)). The close ups in (a) and (c)-(e) are intended to show the high irregularity in vesicle size and shape, and the high degree of interconnections between vesicles. The close up in (e) also shows the high number of small vesicles at the initiation of the lower vesicular lens.

164x76mm (300 x 300 DPI)

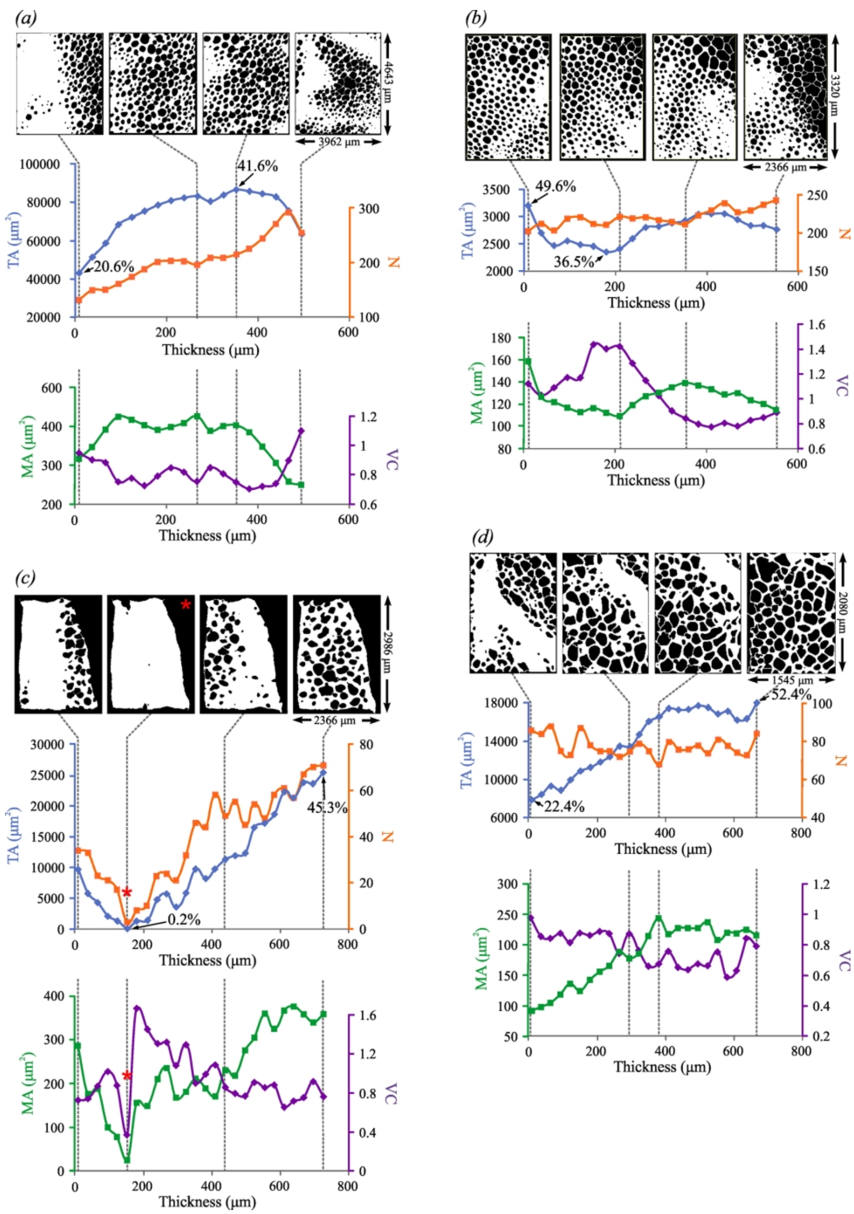

Figure 6. Evolution across the shell thickness of the mentioned parameters: total area occupied by vesicles (TA), number of vesicles (N), mean area of vesicles (MA) and coefficient of variation of the areas of individual vesicles (VC) in selected areas (see dimensions above each graph) of (a) Hyotissa hyotis 1, (b) Hyotissa hyotis 2, (c) Hyotissa sp., and (d) Neopycnodonte cochlear. Note general positive covariation between TA and MA, and negative covariation between MA and VC. The position indicated with an asterisk in (c) is an anomalous value (see text). The top images are digitized micro-CT images taken at different depths (void areas in black and walls in white). Percentages associated to the TA curves are the percent of TA with respect to the whole framed area. Increase in thickness is towards the internal surface of the shell in all cases.

153x218mm (300 x 300 DPI)

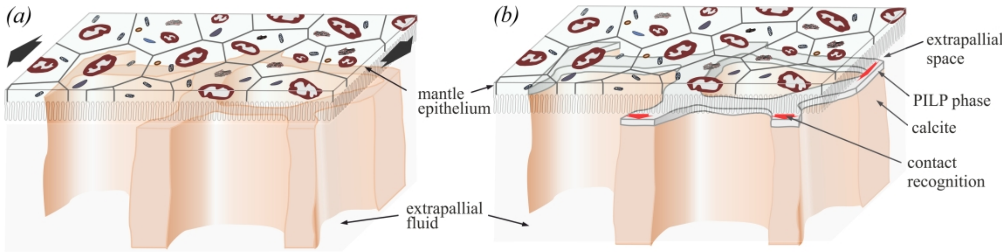

Figure 7. Model for the fabrication of the vesicular materials in gryphaeids. During the oyster's life, the vesicles are infilled with extrapallial fluid. (a) During non-secretory periods, the mantle is able to move with respect to the growth surface of the vesicular shell material (black wide arrows). (b) When shell growth resumes, the mantle cells adhere to the growth surface. Then, they are able to sense the grid formed by the growth ends of the walls (red arrows) and secrete a PILP phase directly and exclusively onto them. With time the PILP crystallizes into calcite.

154x38mm (600 x 600 DPI)

Table 2. Pearson correlation coefficients (r) and probability values (p) for the parameters measured in the four samples examined with micro-CT. See also figure 6. MA: Mean area of vesicles, n: number of data, N: number of vesicles, TA: Total area covered by vesicles, VC: Coefficient of variation.

	TA		N		MA	
	r	p	r	p	r	p
H. hyotis 1 (n= 18)						
N	0.600	0.009				
MA	0.341	0.166	-0.536	0.022		
VC	-0.646	0.004	-0.029	0.909	-0.639	0.004
H. hyotis 2 (n= 20)						
N	0.271	0.248				
MA	0.844	<0.00001	-0.285	0.224		
VC	-0.787	<0.00001	-0.513	0.021	-0.488	0.029
H. sp. (n= 26)						
N	0.931	<0.00001				
MA	0.921	<0.00001	0.813	0.000		
VC	-0.426	0.029	-0.397	0.045	-0.244	0.231
H. sp., removing datum number 6 (indicated with asterisks in figure 6) (n= 25)						
N	0.929	<0.00001				
MA	0.927	<0.00001	0.779	0.000		
VC	-0.620	<0.00001	-0.660	0.000	-0.529	0.007
N. cochlear (n= 24)						
N	-0.358	0.086				
MA	0.976	<0.00001	-0.542	0.006		
VC	-0.792	<0.00001	0.398	0.054	-0.807	<0.00001